NEOWISE REACTIVATION MISSION YEAR ONE: PRELIMINARY ASTEROID DIAMETERS AND ALBEDOS

C. R. Nugent[1], A. Mainzer[2], J. Masiero[2], J. Bauer[2], R. M. Cutri[1], T. Grav[3], E. Kramer[2], S. Sonnett[2], R. Stevenson[2], and
E. L. Wright[4]

[1] Infrared Processing and Analysis Center, California Institute of Technology, Pasadena, CA 91125, USA; cnugent@ipac.caltech.edu
[2] Jet Propulsion Laboratory, California Institute of Technology, Pasadena, CA 91109, USA
[3] Planetary Science Institute, Tucson, AZ, USA
[4] Department of Physics and Astronomy, University of California, Los Angeles, CA 90095, USA
Received 2015 June 11; accepted 2015 September 4; published 2015 November 24

ABSTRACT

We present preliminary diameters and albedos for 7956 asteroids detected in the first year of the *NEOWISE* Reactivation mission. Of those, 201 are near-Earth asteroids and 7755 are Main Belt or Mars-crossing asteroids. 17% of these objects have not been previously characterized using the *Near-Earth Object Wide-field Infrared Survey Explorer*, or "*NEOWISE*" thermal measurements. Diameters are determined to an accuracy of ~20% or better. If good-quality *H* magnitudes are available, albedos can be determined to within ~40% or better.

Key words: minor planets, asteroids: general

Supporting material: machine-readable tables

1. INTRODUCTION

Sizes and albedos of asteroids are basic quantities that can be used to answer a range of scientific questions. A significant number of diameter measurements produce a size–frequency distribution, which can constrain models of asteroid formation and evolution (Zellner 1979; Gradie & Tedesco 1982; Bus & Binzel 2002; Tedesco et al. 2002; Masiero et al. 2011). Asteroid albedos aid the identification of collisional family members (Carruba et al. 2013; Masiero et al. 2013, 2015; Walsh et al. 2013; Milani et al. 2014), and allow for basic characterization of asteroid composition (Mainzer et al. 2011c; Grav et al. 2012a; Masiero et al. 2014).

Most observations of asteroids are made in visible wavelengths, where flux is dependent on both size and albedo. Observations in other wavelengths, such as the infrared (e.g., Hansen 1976; Cruikshank 1977; Lebofsky et al. 1978; Morrison & Lebofsky 1979; Delbó et al. 2003, 2011; Wolters et al. 2005, 2008; Matter et al. 2011; Müller et al. 2012, 2013) or radio (e.g., Ostro et al. 2002; Benner et al. 2015), are needed to determine these quantities precisely. At present, well-determined diameters and albedos have been measured for less than a quarter of known asteroids.

The infrared *NEOWISE* project (Mainzer et al. 2011a) has measured diameters and albedos for ~20% of the known asteroid population, the majority of these measurements to date (Grav et al. 2011, 2012c; Mainzer et al. 2011b, 2012, 2015; Masiero et al. 2011, 2012; Bauer et al. 2013). Here, we expand the number of asteroids characterized by *NEOWISE*, deriving diameters and albedos for asteroids detected by *NEOWISE* between 2013 December 13 and 2014 December 13 during the first year of the Reactivation mission.

The *NEOWISE* mission uses the *Wide-field Infrared Survey Explorer* (*WISE*) spacecraft, which images the entire sky using freeze-frame scanning from a Sun-synchronous polar orbit (Wright et al. 2010; Cutri et al. 2012). *WISE* is equipped with a 50 cm telescope and four 1024×1024 pixel focal plane array detectors that simultaneously image the same 47×47 arcmin field of view in 3.4, 4.6, 12, and 22 μm bands, all originally cooled by solid hydrogen cryogen. *WISE* scans the sky between the ecliptic poles continuously during its 95 minute orbit. A

tertiary scan mirror freezes the sky on the focal planes for 11 s while the detectors are read out, producing a sequence of adjacent images with 7.7 s exposure times in the 3.4 and 4.6 μm bands and 8.8 s in the 12 and 22 μm bands. The orbit precesses at an average rate of approximately one degree per day, so that the full sky is covered in six months.

WISE was launched on 2009 December 14 and began surveying on 2010 January 7. *WISE* scanned the sky 1.5 times during the 9.5 months while it was cooled by its hydrogen cryogen. After the hydrogen was depleted, the survey continued as *NEOWISE* until 2011 February 1, using the 3.4 and 4.6 μm detectors that operated at near full sensitivity with purely passive cooling. During the additional four months of "post-cryo" operations, coverage of the entire inner Main Asteroid Belt was completed, along with a second complete coverage of the sky. *WISE/NEOWISE* was placed into hibernation in 2011 mid-February. In this mode, the solar panels were held facing the Sun and the telescope pointed toward the north ecliptic pole. The telescope viewed the Earth during half of each orbit, resulting in some heating.

The *WISE* spacecraft was brought out of hibernation in 2013 September and renamed *NEOWISE* to continue its mission to discover, track, and characterize asteroids through ~2017 (Mainzer et al. 2014). The telescope was restored to near zenith pointing, which enabled the optics and focal planes to cool passively back to ~74 K. Survey operations resumed on 2013 December 13, with the 3.4 and 4.6 μm detectors operating at a sensitivity comparable to that during the original *WISE* cryogen survey (Cutri et al. 2015). The *NEOWISE* moniker, an acronym of near-Earth object *WISE*, encompasses both the archiving of individual images to allow for the detection of transient objects, and the extensions of the mission beyond *WISE*'s original 9-month lifetime.

NEOWISE uses the same survey and observing strategy as the original *WISE* mission (Wright et al. 2010). The majority of each orbit is devoted to observations, with only brief breaks for data transmission and momentum unloading. The spacecraft carries a body-fixed antenna, and therefore must reorient itself to communicate with the Tracking and Data Relay Satellite System, which relays the data to Earth. Data transmission is
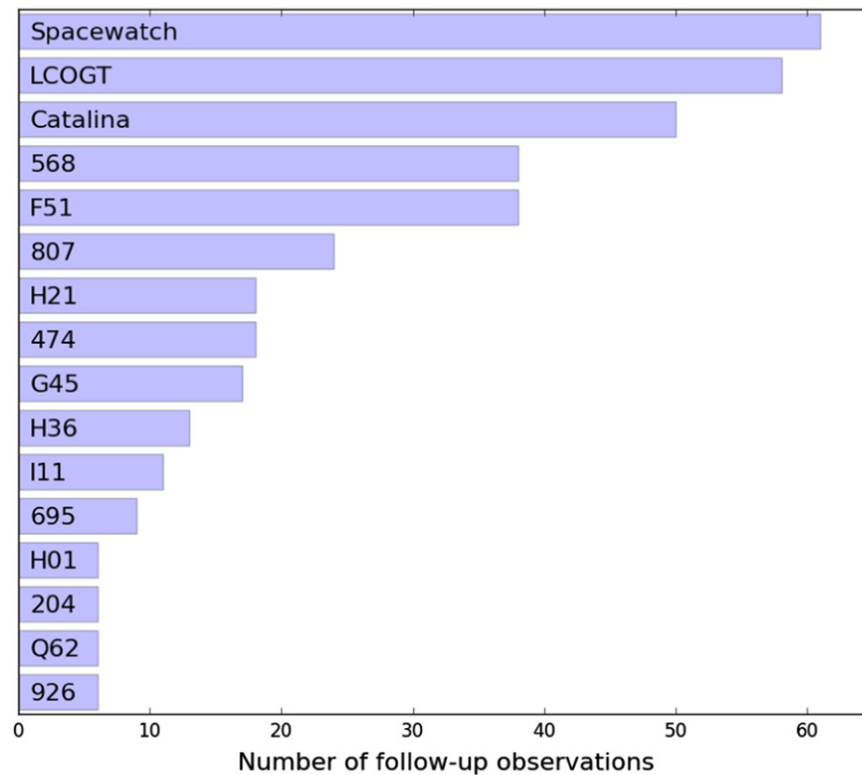
Figure 1. Number of follow-up observations by observatories that contributed >5 observations during the Year 1 Reactivation. Spacewatch, LCOGT, and Catalina employ multiple telescopes; their observatory codes have been grouped together. Observatory code 568, Mauna Kea, is frequently used by the Tholen group.

timed to only interrupt survey coverage near the ecliptic poles, which are observed frequently. Momentum unloading, which can result in streaked images, is also completed at this time.

Data processing for *NEOWISE* uses the *WISE* Science Data System (Cutri et al. 2015), which performs instrumental, photometric, and astrometric calibration for each individual set of 3.4 and 4.6 μm exposures obtained by the spacecraft, and detects and characterizes sources on each exposure. The calibrated images and the database of positions and fluxes of sources extracted from those images for the first year of *NEOWISE* survey observations were released in 2015 March (Cutri et al. 2015).

The *WISE* Moving Object Pipeline System (WMOPS; Cutri et al. 2012) identifies sources that display motion between the different observations of the same region on the sky. WMOPS uses the extracted source lists from sets of images to first identify and filter out sources that appear stationary between individual exposures, and then links non-stationary detections into sets that exhibit physically plausible motion on the sky. Generally, objects within 70 AU of the Sun move quickly enough to be detected by WMOPS (Mainzer et al. 2011a, see also Bauer et al. 2013). Those candidate moving objects that are not associated with known asteroids, comets, planets, or planetary satellites are verified individually by *NEOWISE* scientists. A minimum of five independent detections are required for a tracklet (a set of position/time pairs) to be considered reliable. Tracklets for each verified new candidate object and previously known solar system objects are reported to the IAU Minor Planet Center (MPC) three times per week. The MPC performs initial orbit determination, associates the *NEOWISE* tracklets with known objects, and archives the *NEOWISE* astrometry and times in its observation database.

Candidates confirmed by the MPC to be possible new near-Earth-objects (NEOs) are posted to their NEO Confirmation page for prompt follow-up observations by ground-based observers. Rapid follow-up is essential for *NEOWISE* NEO candidates because the *NEOWISE* arcs are usually short, and the asteroid's projected positional uncertainties grow quickly, making reliable recovery difficult after 2–3 weeks. To ensure prompt follow-up, *NEOWISE* observations are reported to the MPC less than three days after observations on board the spacecraft. A *NEOWISE* candidate discovery has a minimum of five observations over ∼3 hr, although typical objects have ∼12 observations spanning ∼1.5 days.

Targets observed by *NEOWISE* can pose unique challenges to ground-based follow-up observers. *NEOWISE*'s orbit allows observations to be made at all declinations, and observing is independent of lunar phase. Ground-based observers are limited to a fixed declination range, and must sometimes deal with light from the moon and terrestrial weather, which can preclude observations. Moreover, *NEOWISE* discoveries are frequently extremely dark (see Figure 5), often requiring 2–4 m class telescopes to detect them at low solar elongations.

Observers around the globe (including both amateurs and professionals) have contributed essential follow-up observations, which are defined here as an observation of an object within 15 days of its first observation on board the spacecraft. Significant contributors of follow-up observations are given in Figure 1. The Spacewatch Project (McMillan 2007) contributes a large share of recoveries in the northern hemisphere. The Las Cumbres Observatory Global Telescope (LCOGT) Network of robotically operated queue-scheduled telescopes (Brown et al. 2013) has been an extremely useful resource for securing detections when weather is poor at a particular site.

Additionally, the group led by D. Tholen using the University of Hawaii 2.2 m and Canada–France–Hawaii 4 m telescopes has successfully detected the targets with the faintest optical magnitudes in the northern hemisphere (e.g., Tholen et al. 2014). The *NEOWISE* team was awarded time with the DECam instrument on the Cerro Tololo Inter-American Observatory 4 m telescope, which has proven invaluable for the recovery of low albedo objects at extreme declinations in the southern hemisphere.

We present diameters and albedos for 201 near-Earth asteroids (NEAs) and 7755 Main Belt and Mars-crossing asteroids detected in the first year of reactivation, between 2013 December 13 and 2014 December 13. This includes the 38 NEAs discovered by *NEOWISE* during those dates.

2. METHODS

2.1. Observations

The MPC is responsible for verifying and archiving asteroid astrometry. To obtain the verified record of objects found by the WMOPS pipeline in the *NEOWISE* data, we queried the MPC observations files "NumObs.txt" and "UnnObs.txt" for *NEOWISE* (observatory code C51) observations between 2013 December 13 and 2014 December 13. This returned the list of object identifications, along with the observation times and *NEOWISE* measured astrometry. This included known objects and WMOPS asteroid discoveries made during that time.

The NASA/IPAC Infrared Science Archive (IRSA, at http://irsa.ipac.caltech.edu) *NEOWISE-R* Single Exposure Source Table was then queried for the fluxes of sources detected in the *NEOWISE* data. The list of detections extracted from the MPC files was converted into GATOR format (see http://irsa.ipac.caltech.edu/applications/Gator/GatorAid/irsa/QuickGuidetoGator.htm), and uploaded into the IRSA interface using a cone search radius of 2 arcsec and a restriction that times match the MPC-archived observation time to within 2 s. This two-step process of querying both the MPC archive and the *NEOWISE-R* Single Exposure (L1b) Source Table ensures that only detections verified both by the *NEOWISE* object identification routines and the MPC are used for thermal modeling. While there may be additional objects in the database that were detected fewer than five times, or are just below the single-frame detection threshold, this method of extracting moving object detections ensures high reliability, since WMOPS actively works to exclude fixed sources such as stars and galaxies from tracklets. Sources with fewer than five detections or those that fall just below the single-frame detection threshold will be extracted in future processing.

NEOWISE detections were further filtered using several measurement and image quality flags. We required detections to have "ph_qual" values of "A," "B," or "C," "cc_flag" values of "0," and "qual_frame" values of "10." The "ph_qual" flag represents photometric quality, accepting a value of "C" or higher ensures that the sources was detected with a flux signal-to-noise ratio >2. The "cc_flag," or contamination and confusion flag, indicates whether the source measurement may be compromised due to a nearby image artifact. By filtering for "cc_flag" = 0, we select for sources unaffected by known artifacts. Finally, "qual_frame" is an overall quality grade for the entire image in which the source was detected. We accepted only the best-quality images, those with a score of "10."

Table 1
NEOWISE Magnitudes for the NEAs Modeled in This Paper

Name	MJD	W1 (mag)	W2 (mag)	Aperture
01566	56795.5373147	>16.339	13.317 ± 0.086	0
01566	56795.668982	15.340 ± 0.132	13.287 ± 0.104	0
01566	56795.8005219	15.270 ± 0.133	13.255 ± 0.157	0
01566	56795.8663555	15.268 ± 0.137	13.226 ± 0.125	0
01566	56795.9321892	15.590 ± 0.200	13.395 ± 0.166	0
01566	56796.1295626	14.904 ± 0.097	13.348 ± 0.102	0
01566	56796.2612299	15.829 ± 0.192	13.467 ± 0.196	0
01580	56955.905682	>16.484	14.033 ± 0.171	0
01580	56956.037222	>16.124	14.230 ± 0.156	0
01580	56956.431715	17.100 ± 0.538	13.972 ± 0.136	0
01580	56956.5631277	16.951 ± 0.474	14.158 ± 0.198	0
01580	56956.6289614	>16.168	14.159 ± 0.157	0
01580	56956.6946677	16.178 ± 0.252	14.312 ± 0.187	0
01580	56956.7603741	16.442 ± 0.316	13.976 ± 0.154	0
01580	56956.8262078	>17.166	13.988 ± 0.209	0
01580	56956.8919142	16.944 ± 0.523	14.050 ± 0.134	0
01580	56956.9576205	16.206 ± 0.291	14.282 ± 0.186	0
01580	56957.0891606	16.795 ± 0.397	14.271 ± 0.180	0
01580	56957.4179471	>17.009	13.987 ± 0.145	0
01620	56993.9087248	15.427 ± 0.137	14.075 ± 0.156	0
01620	56994.3030911	15.463 ± 0.154	14.049 ± 0.200	0
01620	56994.434504	15.420 ± 0.144	13.556 ± 0.102	0
01620	56994.5659171	15.596 ± 0.171	14.375 ± 0.205	0
01620	56994.5660444	16.012 ± 0.212	14.305 ± 0.221	0
01620	56994.6317509	15.754 ± 0.198	13.846 ± 0.169	0
01620	56994.7631639	15.513 ± 0.145	13.807 ± 0.132	0
01620	56994.8945768	15.794 ± 0.216	14.203 ± 0.228	0
01620	56994.8947042	15.843 ± 0.488	14.106 ± 0.155	0
01620	56994.9604107	15.241 ± 0.129	13.988 ± 0.155	0
01620	56995.0918237	15.203 ± 0.109	13.637 ± 0.140	0
01620	56995.2890705	15.354 ± 0.124	13.483 ± 0.115	0
01620	56995.4204835	15.411 ± 0.161	13.768 ± 0.175	0
01620	56995.8147225	15.912 ± 0.223	14.289 ± 0.205	0

Note. Given are the time of the observation in modified Julian date (MJD), and the magnitude in the 3.4 μm (*W1*) and 4.6 μm bands (*W2*). Non-detections at a particular wavelength represent 95% confidence limits (Cutri et al. 2012). The aperture radius in arcseconds used for aperture photometry is given under "Aperture"; "0" indicates that the pipeline profile fit photometry was used. Only observations for the first three objects are shown.

(This table is available in its entirety in machine-readable form.)

The filtered data from the *NEOWISE* Single Exposure Source Table are high-quality source measurements that were found at the times and locations of *NEOWISE* WMOPS detections submitted to the MPC. To further guard against the possibility of confusing a minor planet with fixed background sources such as stars and galaxies, we uploaded the filtered data to the IRSA catalog query engine, referencing the *WISE* All-sky Source Catalog to determine if any single-frame detections fell within 6.5 arcsec of an Atlas source. The *WISE* Source Catalog is generated using multiple independent single exposure images. Fast-moving solar system objects are suppressed during the construction of the catalog. A search radius of 6.5 arcsec was chosen, as it is the approximate size of the *WISE* beam in the 3.4 and 4.6 μm bands.

We required at least three observations with magnitude errors $\sigma_{mag} \leqslant 0.25$ in one band. The largest main-belt asteroids (MBAs) can saturate the *NEOWISE* detectors, resulting in
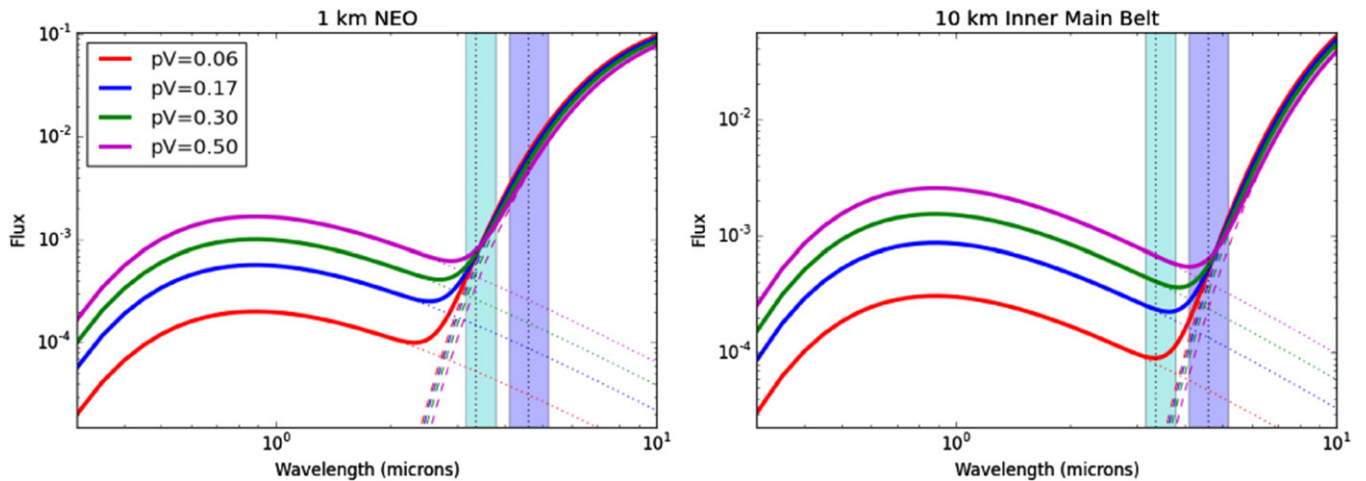
Figure 2. Comparison of spectral energy distribution for a simulated NEO and inner main-belt asteroid, each with albedos ranging from $p_V = 0.06$ to $p_V = 0.5$. Thick lines show the flux from the asteroid as a function of wavelength, which is composed of both thermally emitted (dashed) and reflected sunlight (dotted) components. *NEOWISE* bands centered at 3.4 and 4.6 μm are shown as shaded cyan and purple bars, respectively. For NEAs (left), the 3.4 and 4.6 μm bands are both thermally dominated. For objects in the inner Main Belt (right), the 3.4 μm band is dominated by reflected light, and the 4.6 μm band is dominated by thermally emitted light, though the ratio between these components varies with albedo.

reduced photometric accuracy. Following the prescription laid out in Cutri et al. (2012) (Section IV.4), we did not consider objects that were brighter than 8.0 mag at 3.4 μm and 7.0 mag at 4.6 μm. The NEA measurements used in this work are given in Table 1.

2.2. Near-Earth Thermal Model (NEATM)

We used the NEATM of Harris (1998), following the implementation of Mainzer et al. (2011b, 2012) for NEAs and Masiero et al. (2011, 2012) for MBAs and Mars crossers. These results supersede those published in Mainzer et al. (2014). NEATM is a simple but effective method for determining effective spherical diameters and albedos (when corresponding visible light observations are available). This model makes several assumptions, including a spherical, non-rotating body, with a simple temperature distribution:

$$T(\theta) = T_{\max} \cos^{1/4}(\theta) \quad \text{for} \quad 0 \leqslant \theta \leqslant \pi/2 \qquad (1)$$

where θ is the angular distance from the sub-solar point. $T_{\max}$ is the subsolar temperature, defined as:

$$T_{\max} = \left(\frac{(1 - A)S}{\eta \epsilon \sigma} \right)^{1/4} \qquad (2)$$

where A is the bolometric Bond albedo, S is the solar flux at the asteroid, η is termed the beaming parameter, ϵ is the emissivity, and σ is the Stefan–Boltzmann constant. The beaming parameter η accounts for any deviation between the actual asteroid and the model. Changes in η can account for a host of factors, including non-spherical shapes, the presence of satellites, variations in surface roughness or thermal inertia, uncertainties in emissivity, high rates of spin, changes in surface temperature distributions due to spin pole location, or the imprecise assumption that the object's night-side has zero thermal emission (a factor that is most relevant for objects observed at high phase angles). Some of these factors that are accounted for in the beaming parameter are degenerate. For example, a slow-rotating object will have a heat distribution similar to a faster rotating object that has a lower thermal inertia. For this simple model, beaming accounts for the

changes in temperature distribution due to these effects that cannot be otherwise separated.

Observations were divided into apparitions of 10 days, and the NEATM model was fitted to each individual apparition. These shorter apparitions allowed for fits to widely spaced apparitions or, for NEAs, over changing phase angles. Given that the *NEOWISE* observational cadence generally results in an object being detected over ~1.5 days, sometimes with an additional epoch of observations ~3–6 months later, we chose to divide observations separated by >10 days for separate fitting to account for large changes in object distances and viewing geometries.

NEATM spheres were approximated by a faceted polygon with 800 facets. Individual facet temperature was determined following Equation (1), and then color corrected following Wright et al. (2010). Observed thermal flux for each facet was computed, as was flux from reflected sunlight. The integrated flux from the object was determined, accounting for viewing geometry, to produce a model magnitude. A least-squares fitting routine compared modeled to observed magnitudes, and iterated on diameter, albedo, and beaming parameter until a best fit was found.

Geometric optical albedo p_V was computed using absolute magnitude H and slope parameter G, using values supplied in MPCORB.dat by the MPC. Inaccurate H and G values will result in inaccurate p_V fits. Work by Williams (2012) and Pravec et al. (2012) found systematic H offsets that vary as a function of H magnitude in data reported to the MPC. As albedo measurements depend on H and G values, errors in measurement of those values will propagate to derived albedos.

NEATM requires at least one of the *NEOWISE* wavelengths to be dominated by thermally emitted light. Some outer main-belt objects observed by *NEOWISE* were too cold to have thermally dominated emission at 3.4 or 4.6 μm, and therefore diameters and albedos for those objects are not reported in this paper. The proportion of reflected versus thermally emitted light for NEAs and inner MBAs can be seen in the spectral energy distribution plots shown in Figure 2. The proportion of thermally emitted flux depends on albedo, which means that for colder, outer MBAs it is unclear if a wavelength is thermally

Table 2
Measured Diameters (d) and albedos (p_V) of Near-Earth Objects Not Previously Characterized Using *NEOWISE* Data

Name	Packed	H	G	d (km)	p_V	η	W2 amp.	n_{W1}	n_{W2}
1566	01566	16.90	0.15	1.03 ± 0.04	0.29 ± 0.05	1.40 ± 0.00	0.24	5	7
1580	01580	14.50	0.15	8.55 ± 5.23	0.04 ± 0.08	1.40 ± 0.52	0.34	0	12
1620	01620	15.60	0.15	1.87 ± 0.05	0.29 ± 0.04	1.40 ± 0.00	0.89	14	14
1862	01862	16.25	0.09	1.40 ± 0.04	0.29 ± 0.04	1.40 ± 0.00	0.41	10	10
1862	01862	16.25	0.09	1.26 ± 0.04	0.35 ± 0.05	1.40 ± 0.00	0.84	10	10
1917	01917	13.90	0.15	4.99 ± 0.14	0.20 ± 0.03	1.40 ± 0.00	0.58	14	14
1943	01943	15.75	0.15	2.34 ± 0.05	0.16 ± 0.02	1.40 ± 0.00	0.22	30	31
1943	01943	15.75	0.15	2.30 ± 0.04	0.17 ± 0.02	1.40 ± 0.00	0.29	171	172
1943	01943	15.75	0.15	2.28 ± 0.05	0.17 ± 0.03	1.40 ± 0.00	0.54	14	15
2062	02062	16.80	0.15	0.80 ± 0.03	0.52 ± 0.10	1.40 ± 0.00	0.82	32	36
3288	03288	15.20	0.15	2.49 ± 0.07	0.24 ± 0.04	1.40 ± 0.00	1.40	11	11
4954	04954	12.60	0.15	9.56 ± 0.24	0.18 ± 0.03	1.40 ± 0.00	1.06	8	8
5381	05381	16.50	0.15	0.91 ± 0.05	0.54 ± 0.07	1.40 ± 0.00	0.49	10	10
5381	05381	16.50	0.15	0.94 ± 0.04	0.51 ± 0.06	1.40 ± 0.00	0.17	13	13
6053	06053	14.90	0.15	3.72 ± 0.08	0.14 ± 0.02	1.40 ± 0.00	0.21	11	11
7025	07025	18.30	0.15	0.50 ± 0.17	0.34 ± 0.23	1.40 ± 0.52	0.58	0	4
7889	07889	15.20	0.15	1.68 ± 0.07	0.52 ± 0.06	1.40 ± 0.00	0.45	8	8
8567	08567	15.30	0.15	2.93 ± 0.07	0.16 ± 0.03	1.40 ± 0.00	0.42	25	26
13651	13651	17.60	0.15	0.56 ± 0.02	0.51 ± 0.11	1.40 ± 0.00	1.22	11	11
35107	35107	16.80	0.15	0.91 ± 0.03	0.41 ± 0.05	1.40 ± 0.00	0.25	10	10
35107	35107	16.80	0.15	1.10 ± 0.28	0.28 ± 0.16	1.40 ± 0.37	0.45	0	14
39572	39572	16.50	0.15	1.55 ± 0.66	0.18 ± 0.16	1.40 ± 0.47	0.42	0	8
39796	39796	15.70	0.15	2.13 ± 0.59	0.20 ± 0.20	1.40 ± 0.39	0.69	0	16
53430	53430	16.60	0.15	1.23 ± 0.32	0.27 ± 0.15	1.40 ± 0.37	1.14	0	5
54686	54686	16.50	0.15	1.35 ± 0.46	0.24 ± 0.19	1.40 ± 0.47	1.02	0	10
55532	55532	16.10	0.15	1.31 ± 0.04	0.38 ± 0.06	1.40 ± 0.00	0.22	6	6
68063	68063	15.50	0.15	2.30 ± 0.07	0.21 ± 0.04	1.40 ± 0.00	0.38	24	24
68267	68267	16.90	0.15	0.88 ± 0.04	0.40 ± 0.05	1.40 ± 0.00	0.29	13	15
68348	68348	14.20	0.15	3.51 ± 0.13	0.30 ± 0.05	1.40 ± 0.00	0.46	12	12
68548	68548	16.50	0.15	1.18 ± 0.04	0.32 ± 0.04	1.40 ± 0.00	0.24	8	10
68548	68548	16.50	0.15	1.24 ± 0.04	0.29 ± 0.03	1.40 ± 0.00	0.55	23	24
85182	85182	17.10	0.15	1.03 ± 0.37	0.24 ± 0.19	1.40 ± 0.49	0.69	0	9
85774	85774	19.20	0.15	0.94 ± 0.01	0.04 ± 0.01	1.40 ± 0.00	0.90	11	11
86819	86819	17.40	0.15	0.80 ± 0.27	0.30 ± 0.22	1.40 ± 0.46	0.79	0	7
86829	86829	15.90	0.15	1.43 ± 0.05	0.37 ± 0.05	1.40 ± 0.00	0.33	14	14
87309	87309	17.60	0.15	0.57 ± 0.16	0.50 ± 0.23	1.40 ± 0.47	0.67	0	10
88213	88213	19.70	0.15	0.91 ± 0.42	0.03 ± 0.03	1.40 ± 0.51	0.66	0	6
89355	89355	15.60	0.15	2.04 ± 0.05	0.25 ± 0.03	1.40 ± 0.00	1.19	30	31
90075	90075	15.20	0.15	2.23 ± 0.08	0.29 ± 0.04	1.40 ± 0.00	0.73	12	12
99248	99248	16.30	0.15	1.12 ± 0.04	0.43 ± 0.06	1.40 ± 0.00	0.29	7	8
99248	99248	16.30	0.15	1.14 ± 0.37	0.41 ± 0.28	1.40 ± 0.48	0.48	0	8
137099	D7099	18.20	0.15	0.56 ± 0.02	0.29 ± 0.04	1.40 ± 0.00	0.65	6	6
138127	D8127	17.10	0.15	0.75 ± 0.02	0.45 ± 0.06	1.40 ± 0.00	0.17	7	7
138947	D8947	18.70	0.15	0.45 ± 0.12	0.29 ± 0.28	1.40 ± 0.46	0.46	0	9
142781	E2781	16.10	0.15	1.59 ± 0.05	0.25 ± 0.04	1.40 ± 0.00	0.15	14	14
142781	E2781	16.10	0.15	2.01 ± 0.74	0.16 ± 0.15	1.40 ± 0.44	0.85	0	15
142781	E2781	16.10	0.15	2.03 ± 0.77	0.16 ± 0.09	1.40 ± 0.40	0.45	0	9
143624	E3624	15.90	0.15	2.14 ± 0.04	0.17 ± 0.03	1.40 ± 0.00	0.32	9	9
143624	E3624	15.90	0.15	2.23 ± 1.08	0.15 ± 0.17	1.40 ± 0.53	0.82	0	8
154276	F4276	17.60	0.15	1.06 ± 0.35	0.14 ± 0.17	1.40 ± 0.43	0.29	0	5
159454	F9454	17.90	0.15	0.58 ± 0.02	0.37 ± 0.04	1.40 ± 0.00	0.30	6	6
159560	F9560	17.00	0.15	1.10 ± 0.47	0.24 ± 0.23	1.40 ± 0.54	1.16	0	87
159560	F9560	17.00	0.15	1.16 ± 0.30	0.21 ± 0.21	1.40 ± 0.39	0.53	0	13
159857	F9857	15.40	0.15	3.07 ± 1.32	0.13 ± 0.16	1.40 ± 0.45	0.34	0	5
162058	G2058	17.80	0.15	0.85 ± 0.01	0.19 ± 0.02	1.40 ± 0.00	0.34	26	27
162058	G2058	17.80	0.15	0.85 ± 0.28	0.19 ± 0.14	1.40 ± 0.44	0.87	0	31
162080	G2080	19.80	0.15	0.78 ± 0.06	0.04 ± 0.01	1.40 ± 0.11	1.39	4	4
162080	G2080	19.80	0.15	0.82 ± 0.33	0.03 ± 0.07	1.40 ± 0.49	0.99	0	13
162116	G2116	19.30	0.15	0.54 ± 0.17	0.12 ± 0.08	1.40 ± 0.40	0.47	0	7
162567	G2567	19.90	0.15	0.33 ± 0.01	0.17 ± 0.03	1.40 ± 0.00	0.20	6	6
162741	G2741	17.30	0.15	3.95 ± 0.04	0.01 ± 0.00	1.40 ± 0.00	0.22	6	6
162980	G2980	16.70	0.15	0.79 ± 0.04	0.66 ± 0.13	1.40 ± 0.00	0.40	8	8
163818	G3818	18.40	0.15	0.39 ± 0.02	0.52 ± 0.06	1.40 ± 0.00	0.33	7	7
172034	H2034	17.80	0.15	0.63 ± 0.02	0.34 ± 0.05	1.40 ± 0.00	1.05	16	16
190166	J0166	17.10	0.15	1.01 ± 0.03	0.25 ± 0.04	1.40 ± 0.00	0.92	6	7

Table 2
(Continued)

Name	Packed	H	G	d (km)	p_V	η	W2 amp.	n_{W1}	n_{W2}
190166	J0166	17.10	0.15	1.05 ± 0.02	0.23 ± 0.03	1.40 ± 0.00	0.68	12	12
209924	K9924	16.10	0.15	1.86 ± 0.71	0.19 ± 0.12	1.40 ± 0.44	0.40	0	7
211871	L1871	18.80	0.15	0.41 ± 0.01	0.32 ± 0.05	1.40 ± 0.00	0.28	5	7
214088	L4088	15.20	0.15	2.42 ± 0.06	0.25 ± 0.03	1.40 ± 0.00	0.63	8	8
215588	L5588	19.50	0.15	0.49 ± 0.16	0.12 ± 0.12	1.40 ± 0.44	0.57	0	5
215757	L5757	17.70	0.15	0.78 ± 0.27	0.24 ± 0.17	1.40 ± 0.48	0.47	0	11
235086	N5086	17.50	0.15	1.02 ± 0.40	0.17 ± 0.18	1.40 ± 0.51	1.04	0	60
235086	N5086	17.50	0.15	1.02 ± 0.32	0.17 ± 0.11	1.40 ± 0.38	1.64	0	32
235086	N5086	17.50	0.15	1.08 ± 0.33	0.15 ± 0.12	1.40 ± 0.38	0.85	0	29
242450	O2450	14.70	0.15	2.54 ± 0.10	0.36 ± 0.13	1.40 ± 0.00	0.41	11	11
242450	O2450	14.70	0.15	2.91 ± 0.08	0.27 ± 0.04	1.40 ± 0.00	0.83	13	14
250620	P0620	18.00	0.15	0.65 ± 0.14	0.26 ± 0.13	1.40 ± 0.33	0.29	0	4
267337	Q7337	18.00	0.15	0.44 ± 0.10	0.58 ± 0.25	1.40 ± 0.43	0.21	0	4
269690	Q9690	18.40	0.15	0.89 ± 0.43	0.10 ± 0.11	1.40 ± 0.59	0.31	0	7
271480	R1480	17.50	0.15	0.71 ± 0.22	0.35 ± 0.22	1.40 ± 0.48	0.82	0	6
274138	R4138	17.80	0.15	0.75 ± 0.02	0.24 ± 0.03	1.40 ± 0.00	0.48	7	7
275976	R5976	16.30	0.15	1.86 ± 0.04	0.15 ± 0.03	1.40 ± 0.00	1.01	5	5
275976	R5976	16.30	0.15	2.38 ± 0.03	0.09 ± 0.01	1.40 ± 0.00	1.11	15	16
276274	R6274	17.20	0.15	1.53 ± 0.71	0.10 ± 0.17	1.40 ± 0.52	0.91	0	5
276468	R6468	17.90	0.15	1.03 ± 0.37	0.11 ± 0.14	1.40 ± 0.42	0.36	0	5
285944	S5944	16.50	0.15	1.04 ± 0.04	0.41 ± 0.03	1.40 ± 0.00	0.16	10	10
285944	S5944	16.50	0.15	1.40 ± 0.43	0.23 ± 0.19	1.40 ± 0.41	0.51	0	29
297418	T7418	18.60	0.15	0.41 ± 0.02	0.39 ± 0.05	1.40 ± 0.00	0.93	5	5
299582	T9582	18.00	0.15	0.62 ± 0.02	0.29 ± 0.03	1.40 ± 0.00	0.31	7	7
303174	U3174	16.70	0.15	1.50 ± 0.03	0.16 ± 0.03	1.40 ± 0.00	0.65	21	23
304330	U4330	18.90	0.15	0.61 ± 0.01	0.13 ± 0.02	1.40 ± 0.00	0.13	11	11
304330	U4330	18.90	0.15	0.78 ± 0.01	0.08 ± 0.01	1.40 ± 0.00	0.23	12	12
322763	W2763	16.90	0.15	1.25 ± 0.03	0.20 ± 0.04	1.40 ± 0.00	0.27	12	13
326388	W6388	18.20	0.15	1.26 ± 0.57	0.06 ± 0.12	1.40 ± 0.52	0.33	0	8
334673	X4673	17.90	0.15	0.57 ± 0.22	0.38 ± 0.25	1.40 ± 0.60	0.67	0	11
349219	Y9219	18.20	0.15	0.58 ± 0.15	0.27 ± 0.23	1.40 ± 0.41	0.58	0	14
363505	a3505	18.10	0.15	1.90 ± 0.05	0.03 ± 0.01	1.40 ± 0.03	0.66	12	12
368184	a8184	19.50	0.15	0.38 ± 0.12	0.19 ± 0.19	1.40 ± 0.46	0.54	0	25
369264	a9264	16.30	0.15	1.51 ± 0.47	0.23 ± 0.20	1.40 ± 0.42	0.65	0	7
377732	b7732	17.00	0.15	0.95 ± 0.03	0.31 ± 0.05	1.40 ± 0.00	0.62	5	5
377732	b7732	17.00	0.15	0.99 ± 0.03	0.29 ± 0.03	1.40 ± 0.00	0.16	5	5
381677	c1677	18.40	0.15	0.47 ± 0.01	0.35 ± 0.05	1.40 ± 0.00	0.92	19	19
381677	c1677	18.40	0.15	0.44 ± 0.16	0.40 ± 0.21	1.40 ± 0.54	0.47	0	5
387733	c7733	18.90	0.15	0.34 ± 0.01	0.41 ± 0.06	1.40 ± 0.00	0.22	11	11
387733	c7733	18.90	0.15	0.32 ± 0.09	0.47 ± 0.25	1.40 ± 0.46	0.37	0	5
387746	c7746	20.00	0.15	0.37 ± 0.01	0.13 ± 0.02	1.40 ± 0.00	0.23	5	6
388838	c8838	19.50	0.15	0.36 ± 0.01	0.21 ± 0.04	1.40 ± 0.00	0.61	18	18
388838	c8838	19.50	0.15	0.38 ± 0.01	0.20 ± 0.02	1.40 ± 0.00	0.24	12	12
389694	c9694	18.20	0.15	0.45 ± 0.02	0.46 ± 0.06	1.40 ± 0.00	0.22	4	5
391211	d1211	18.50	0.15	0.41 ± 0.09	0.42 ± 0.23	1.40 ± 0.38	0.85	0	17
393359	d3359	19.20	0.15	0.77 ± 0.33	0.06 ± 0.11	1.40 ± 0.52	0.51	0	30
393569	d3569	20.20	0.15	0.55 ± 0.01	0.05 ± 0.01	1.40 ± 0.00	0.22	13	14
399433	d9433	18.60	0.15	1.34 ± 0.56	0.04 ± 0.09	1.40 ± 0.49	0.24	0	10
399433	d9433	18.60	0.15	1.76 ± 0.89	0.02 ± 0.05	1.40 ± 0.53	0.16	0	9
406952	e6952	17.10	0.15	0.77 ± 0.21	0.43 ± 0.23	1.40 ± 0.44	0.64	0	5
408751	e8751	19.00	0.15	0.40 ± 0.01	0.28 ± 0.03	1.40 ± 0.00	0.84	68	69
409256	e9256	18.20	0.15	1.89 ± 0.68	0.03 ± 0.04	1.40 ± 0.40	0.84	0	4
409836	e9836	18.10	0.15	0.55 ± 0.19	0.33 ± 0.25	1.40 ± 0.49	1.78	0	14
410088	f0088	18.10	0.15	1.03 ± 0.01	0.10 ± 0.02	1.40 ± 0.00	0.14	9	10
410778	f0778	18.10	0.15	1.46 ± 0.57	0.05 ± 0.03	1.40 ± 0.41	0.38	0	6
411201	f1201	17.80	0.15	0.66 ± 0.01	0.31 ± 0.05	1.40 ± 0.00	1.45	12	15
411611	f1611	18.80	0.15	0.36 ± 0.10	0.41 ± 0.21	1.40 ± 0.43	0.81	0	31
413038	f3038	16.90	0.15	1.24 ± 0.03	0.20 ± 0.04	1.40 ± 0.00	1.19	22	23
413038	f3038	16.90	0.15	1.01 ± 0.04	0.30 ± 0.04	1.40 ± 0.00	1.79	23	25
413192	f3192	16.80	0.15	3.96 ± 1.84	0.02 ± 0.05	1.40 ± 0.47	0.62	0	18
413421	f3421	18.30	0.15	1.90 ± 0.78	0.02 ± 0.02	1.40 ± 0.41	1.39	0	23
413820	f3820	19.80	0.15	0.66 ± 0.26	0.05 ± 0.04	1.40 ± 0.46	0.97	0	36
414286	f4286	18.60	0.15	0.37 ± 0.08	0.47 ± 0.19	1.40 ± 0.38	0.54	0	27
414286	f4286	18.60	0.15	0.40 ± 0.09	0.40 ± 0.24	1.40 ± 0.40	0.71	0	29

Table 2
(Continued)

Name	Packed	H	G	d (km)	p_V	η	W2 amp.	n_{W1}	n_{W2}
418797	f8797	19.40	0.15	0.70 ± 0.29	0.06 ± 0.07	1.40 ± 0.50	0.32	0	7
418929	f8929	17.00	0.15	1.43 ± 0.02	0.14 ± 0.03	1.40 ± 0.00	0.54	48	49
419624	f9624	20.50	0.15	0.34 ± 0.14	0.09 ± 0.17	1.40 ± 0.50	0.57	0	18
419624	f9624	20.50	0.15	0.36 ± 0.13	0.09 ± 0.14	1.40 ± 0.46	0.46	0	6
419880	f9880	19.60	0.15	0.98 ± 0.06	0.03 ± 0.01	1.40 ± 0.08	0.20	6	6
2000 AG205	K00AK5G	19.70	0.15	0.95 ± 0.01	0.03 ± 0.00	1.40 ± 0.00	0.79	12	14
2002 XS40	K02X40S	20.10	0.15	0.76 ± 0.03	0.03 ± 0.00	1.40 ± 0.05	0.18	14	14
2003 CC11	K03C11C	19.10	0.15	1.13 ± 0.51	0.03 ± 0.10	1.40 ± 0.53	0.49	0	16
2003 SS214	K03SL4S	20.10	0.15	0.86 ± 0.25	0.02 ± 0.02	1.40 ± 0.35	0.75	0	16
2004 BZ74	K04B74Z	18.10	0.15	0.96 ± 0.02	0.11 ± 0.02	1.40 ± 0.00	0.65	4	5
2004 MX2	K04M02X	19.30	0.15	1.26 ± 0.08	0.02 ± 0.00	1.40 ± 0.09	0.35	9	9
2004 TG10	K04T10G	19.40	0.15	1.32 ± 0.61	0.02 ± 0.04	1.40 ± 0.51	0.64	0	8
2005 LS3	K05L03S	19.50	0.15	0.38 ± 0.10	0.19 ± 0.12	1.40 ± 0.38	0.64	0	7
2006 BB27	K06B27B	20.00	0.15	0.22 ± 0.05	0.38 ± 0.21	1.40 ± 0.38	0.98	0	5
2007 BG	K07B00G	19.50	0.15	0.31 ± 0.11	0.24 ± 0.19	1.40 ± 0.51	0.38	3	5
2007 RU10	K07R10U	19.10	0.15	0.92 ± 0.37	0.05 ± 0.06	1.40 ± 0.47	0.31	0	9
2008 QS11	K08Q11S	19.90	0.15	0.45 ± 0.01	0.09 ± 0.01	1.40 ± 0.00	0.33	9	11
2009 ND1	K09N01D	17.10	0.15	2.50 ± 0.95	0.04 ± 0.04	1.40 ± 0.39	0.70	0	11
2010 OQ1	K10O01Q	19.00	0.15	0.54 ± 0.21	0.15 ± 0.14	1.40 ± 0.51	0.47	0	8
2011 CQ4	K11C04Q	18.40	0.15	0.66 ± 0.02	0.18 ± 0.02	1.40 ± 0.00	0.29	5	7
2012 DN	K12D00N	18.10	0.15	2.77 ± 1.05	0.01 ± 0.03	1.40 ± 0.38	0.42	0	7
2013 PX6	K13P06X	18.40	0.15	1.65 ± 0.03	0.03 ± 0.00	1.40 ± 0.02	0.19	9	10
2013 WT44	K13W44T	19.30	0.15	0.65 ± 0.01	0.08 ± 0.02	1.40 ± 0.00	0.31	6	6
2013 WU44	K13W44U	21.00	0.15	0.29 ± 0.13	0.09 ± 0.19	1.40 ± 0.61	0.26	0	8
2013 YZ13	K13Y13Z	19.60	0.15	0.31 ± 0.10	0.27 ± 0.19	1.40 ± 0.46	0.07	0	6
2013 YP139	K13YD9P	21.60	0.15	0.40 ± 0.03	0.03 ± 0.01	1.09 ± 0.07	0.25	6	6
2014 AA33	K14A33A	19.30	0.15	0.79 ± 0.04	0.05 ± 0.01	1.40 ± 0.06	0.19	4	4
2014 AQ46	K14A46Q	20.10	0.15	0.59 ± 0.29	0.05 ± 0.11	1.40 ± 0.60	0.47	0	17
2014 AA53	K14A53A	19.80	0.15	0.70 ± 0.27	0.04 ± 0.06	1.40 ± 0.47	0.50	0	13
2014 BG60	K14B60G	20.10	0.15	0.67 ± 0.25	0.04 ± 0.08	1.40 ± 0.46	1.30	0	163
2014 BE63	K14B63E	23.20	0.15	0.36 ± 0.13	0.01 ± 0.00	1.40 ± 0.46	0.42	0	5
2014 CY4	K14C04Y	21.10	0.15	0.57 ± 0.25	0.02 ± 0.04	1.40 ± 0.52	0.35	0	5
2014 DC10	K14D10C	20.10	0.15	0.89 ± 0.01	0.02 ± 0.00	1.40 ± 0.00	0.90	9	10
2014 ED	K14E00D	19.30	0.15	0.49 ± 0.13	0.14 ± 0.14	1.40 ± 0.39	0.57	0	6
2014 EN45	K14E45N	21.20	0.15	0.37 ± 0.13	0.04 ± 0.01	0.75 ± 0.24	0.16	12	12
2014 EZ48	K14E48Z	18.80	0.15	0.45 ± 0.01	0.26 ± 0.04	1.40 ± 0.00	1.10	5	6
2014 EZ48	K14E48Z	18.80	0.15	0.44 ± 0.11	0.27 ± 0.21	1.40 ± 0.38	0.47	0	6
2014 EQ49	K14E49Q	21.80	0.15	0.38 ± 0.13	0.02 ± 0.03	1.40 ± 0.42	0.42	0	5
2014 ER49	K14E49R	18.60	0.15	0.46 ± 0.15	0.30 ± 0.26	1.40 ± 0.49	0.51	0	9
2014 HE3	K14H03E	19.90	0.15	0.56 ± 0.15	0.06 ± 0.04	1.40 ± 0.34	0.18	0	5
2014 HQ124	K14HC4Q	18.90	0.15	0.41 ± 0.17	0.29 ± 0.22	1.40 ± 0.57	0.80	0	10
2014 HF177	K14HH7F	19.70	0.15	0.25 ± 0.01	0.36 ± 0.06	1.40 ± 0.00	0.39	10	12
2014 JL25	K14J25L	23.00	0.15	0.23 ± 0.06	0.02 ± 0.03	1.40 ± 0.34	0.68	0	5
2014 JH57	K14J57H	16.60	0.15	4.61 ± 0.03	0.02 ± 0.00	1.40 ± 0.00	0.11	6	6
2014 JH57	K14J57H	16.60	0.15	6.79 ± 3.81	0.01 ± 0.03	1.40 ± 0.47	0.30	0	5
2014 JN57	K14J57N	20.70	0.15	0.27 ± 0.10	0.12 ± 0.10	1.40 ± 0.47	0.69	0	4
2014 KX99	K14K99X	18.20	0.15	1.72 ± 0.68	0.03 ± 0.05	1.40 ± 0.46	0.43	0	9
2014 LQ25	K14L25Q	20.00	0.15	0.94 ± 0.32	0.02 ± 0.01	1.40 ± 0.37	0.48	0	5
2014 LR26	K14L26R	18.50	0.15	2.08 ± 0.90	0.02 ± 0.03	1.40 ± 0.46	0.65	0	6
2014 MQ18	K14M18Q	15.60	0.15	5.27 ± 3.50	0.04 ± 0.07	1.40 ± 0.52	0.54	0	8
2014 NB39	K14N39B	19.50	0.15	1.08 ± 0.15	0.02 ± 0.02	1.40 ± 0.18	0.08	7	7
2014 NE52	K14N52E	17.90	0.15	0.70 ± 0.22	0.25 ± 0.27	1.40 ± 0.47	0.66	0	9
2014 NC64	K14N64C	20.50	0.15	0.50 ± 0.19	0.04 ± 0.02	0.82 ± 0.29	0.64	5	6
2014 NM64	K14N64M	22.60	0.15	0.33 ± 0.12	0.01 ± 0.02	1.40 ± 0.44	0.82	0	25
2014 OY1	K14O01Y	19.10	0.15	0.60 ± 0.21	0.11 ± 0.09	1.40 ± 0.43	0.30	0	6
2014 OZ1	K14O01Z	21.00	0.15	0.73 ± 0.29	0.01 ± 0.03	1.40 ± 0.49	0.38	0	21
2014 PC68	K14P68C	20.40	0.15	0.56 ± 0.20	0.04 ± 0.04	1.40 ± 0.43	0.39	0	8
2014 PF68	K14P68F	18.20	0.15	3.33 ± 2.06	0.01 ± 0.01	1.20 ± 0.48	0.60	0	12
2014 QK433	K14Qh3K	18.30	0.15	1.78 ± 0.75	0.03 ± 0.06	1.40 ± 0.47	0.79	0	10
2014 RH12	K14R12H	23.50	0.15	0.09 ± 0.04	0.09 ± 0.11	1.40 ± 0.54	0.75	0	10
2014 RL12	K14R12L	17.90	0.15	0.69 ± 0.02	0.25 ± 0.03	1.40 ± 0.00	0.31	5	5
2014 RL12	K14R12L	17.90	0.15	0.61 ± 0.17	0.33 ± 0.19	1.40 ± 0.42	0.83	0	6
2014 SR339	K14SX9R	18.60	0.15	0.97 ± 0.37	0.07 ± 0.07	1.40 ± 0.46	0.69	0	13
2014 TW57	K14T57W	20.10	0.15	0.47 ± 0.01	0.07 ± 0.02	1.40 ± 0.00	0.76	4	6

Table 2
(Continued)

Name	Packed	H	G	d (km)	p_V	η	W2 amp.	n_{W1}	n_{W2}
2014 TF64	K14T64F	20.10	0.15	0.70 ± 0.20	0.03 ± 0.03	1.40 ± 0.35	0.33	0	5
2014 TJ64	K14T64J	21.30	0.15	0.52 ± 0.20	0.02 ± 0.02	1.40 ± 0.47	0.46	0	31
2014 TJ64	K14T64J	21.30	0.15	0.52 ± 0.23	0.02 ± 0.03	1.40 ± 0.54	0.55	0	14
2014 UG176	K14UH6G	21.50	0.15	0.42 ± 0.12	0.03 ± 0.03	1.40 ± 0.39	0.17	0	8
2014 US192	K14UJ2S	18.70	0.15	0.87 ± 0.01	0.08 ± 0.01	1.40 ± 0.00	0.25	5	5
2014 UF206	K14UK6F	18.80	0.15	1.63 ± 0.79	0.02 ± 0.04	1.40 ± 0.49	0.62	0	17
2014 UH210	K14UL0H	21.10	0.15	0.40 ± 0.16	0.04 ± 0.06	1.40 ± 0.47	0.76	0	5
2014 VP35	K14V35P	22.70	0.15	0.12 ± 0.05	0.10 ± 0.10	1.40 ± 0.53	0.36	0	6
2014 WJ70	K14W70J	17.60	0.15	2.92 ± 1.21	0.02 ± 0.04	1.40 ± 0.44	0.62	0	27
2014 XQ7	K14X07Q	20.60	0.15	0.65 ± 0.29	0.02 ± 0.05	1.40 ± 0.55	0.83	0	8
2014 XX7	K14X07X	19.80	0.15	1.20 ± 0.38	0.01 ± 0.02	1.40 ± 0.36	0.43	0	6
2014 XX31	K14X31X	17.60	0.15	1.35 ± 0.49	0.09 ± 0.15	1.40 ± 0.43	0.42	0	8

Note. Magnitude H, slope parameter G, and beaming η used are given. The numbers of observations used in the 3.4 μm (n_{W1}) and 4.6 μm (n_{W2}) wavelengths are also reported, along with the amplitude of the 4.6 μm light curve (W2 amp.).

(This table is available in machine-readable form.)

Table 3
Measured Diameters (d) and Albedos (p_V) of Near-Earth Objects Previously Characterized Using *NEOWISE* Data

Name	Packed	H	G	d (km)	p_V	η	W2 Amp.	n_{W1}	n_{W2}
2102	02102	16.00	0.15	1.68 ± 0.05	0.25 ± 0.04	1.40 ± 0.00	0.23	13	13
2102	02102	16.00	0.15	1.65 ± 0.05	0.26 ± 0.04	1.40 ± 0.00	0.18	5	5
2102	02102	16.00	0.15	1.69 ± 0.06	0.25 ± 0.03	1.40 ± 0.00	0.67	8	9
3554	03554	15.82	0.15	1.56 ± 0.07	0.34 ± 0.06	1.40 ± 0.00	0.49	19	20
4183	04183	14.40	0.15	2.94 ± 0.12	0.36 ± 0.06	1.40 ± 0.00	1.04	12	12
4183	04183	14.40	0.15	3.54 ± 0.12	0.24 ± 0.04	1.40 ± 0.00	0.62	17	18
6050	06050	14.80	0.15	2.88 ± 0.07	0.26 ± 0.04	1.40 ± 0.00	1.51	57	57
25916	25916	13.60	0.15	5.96 ± 0.13	0.18 ± 0.03	1.40 ± 0.00	0.63	24	29
27346	27346	15.90	0.15	1.80 ± 0.07	0.24 ± 0.04	1.40 ± 0.00	0.43	9	9
40263	40263	17.70	0.15	0.92 ± 0.35	0.17 ± 0.18	1.40 ± 0.48	0.71	0	14
40267	40267	15.40	0.15	2.39 ± 0.09	0.21 ± 0.04	1.40 ± 0.00	1.06	4	4
85628	85628	17.00	0.15	0.78 ± 0.03	0.46 ± 0.08	1.40 ± 0.00	0.64	7	10
90367	90367	17.70	0.15	1.76 ± 0.79	0.05 ± 0.13	1.40 ± 0.51	0.54	0	12
90367	90367	17.70	0.15	2.00 ± 0.89	0.04 ± 0.03	1.40 ± 0.46	0.49	0	13
137062	D7062	16.60	0.15	0.99 ± 0.06	0.41 ± 0.05	1.40 ± 0.00	0.89	6	6
138847	D8847	16.90	0.15	0.94 ± 0.28	0.35 ± 0.19	1.40 ± 0.44	1.01	0	26
162181	G2181	18.20	0.15	0.73 ± 0.02	0.17 ± 0.03	1.40 ± 0.00	0.32	25	25
162483	G2483	17.50	0.15	0.69 ± 0.20	0.37 ± 0.21	1.40 ± 0.44	0.62	0	9
162566	G2566	15.70	0.15	6.00 ± 2.42	0.03 ± 0.04	1.40 ± 0.40	1.02	0	24
163691	G3691	17.00	0.15	3.06 ± 1.55	0.03 ± 0.06	1.40 ± 0.54	0.30	0	5
243566	O3566	17.40	0.15	0.88 ± 0.02	0.25 ± 0.04	1.40 ± 0.00	0.29	11	11
262623	Q2623	18.50	0.15	0.49 ± 0.15	0.29 ± 0.18	1.40 ± 0.44	0.48	0	4
276049	R6049	16.80	0.15	4.03 ± 1.85	0.02 ± 0.04	1.40 ± 0.44	0.54	0	6
277616	R7616	17.40	0.15	1.28 ± 0.01	0.12 ± 0.02	1.40 ± 0.00	0.28	4	4
395207	d5207	19.60	0.15	0.60 ± 0.20	0.07 ± 0.03	1.40 ± 0.40	0.32	0	8
395207	d5207	19.60	0.15	0.73 ± 0.30	0.05 ± 0.10	1.40 ± 0.49	0.50	0	19
397237	d7237	16.70	0.15	1.73 ± 0.66	0.12 ± 0.16	1.40 ± 0.46	0.40	0	4
1998 SB15	J98S15B	20.90	0.15	0.36 ± 0.12	0.06 ± 0.09	1.40 ± 0.44	0.66	0	11
2009 UX17	K09U17X	21.50	0.15	0.39 ± 0.13	0.03 ± 0.03	1.40 ± 0.40	0.86	0	15
2010 LF86	K10L86F	17.30	0.15	2.30 ± 0.89	0.04 ± 0.04	1.40 ± 0.41	0.21	0	7
2010 LO97	K10L97O	18.70	0.15	1.40 ± 0.57	0.03 ± 0.06	1.40 ± 0.47	0.57	0	15
2010 NG3	K10N03G	17.20	0.15	1.45 ± 0.02	0.11 ± 0.02	1.40 ± 0.00	0.64	17	17
2010 NG3	K10N03G	17.20	0.15	1.74 ± 0.94	0.08 ± 0.18	1.40 ± 0.59	0.80	0	17
2014 HJ129	K14HC9J	21.10	0.15	0.59 ± 0.21	0.02 ± 0.02	1.40 ± 0.42	0.50	0	9

Note. Objects in this table have previously reported measurements by the *NEOWISE* team (Mainzer et al. 2011b, 2012). Previous measurements use detections in the 12 and 22 μm bands, and therefore are better constrained. Magnitude H, slope parameter G, and beaming η used are given. The numbers of observations used in the 3.4 μm (n_{W1}) and 4.6 μm (n_{W2}) wavelengths are also reported, along with the amplitude of the 4.6 μm light curve (W2 amp.).

(This table is available in machine-readable form.)

Table 4
Measured Diameters (d) and Albedos (p_V) of MBAs and Mars Crossers Not Previously Characterized Using *NEOWISE* Data

Name	Packed	H	G	d (km)	p_V	η	W2 Amp.	n_{W1}	n_{W2}
21	00021	7.35	0.11	99.47 ± 27.12	0.16 ± 0.12	0.95 ± 0.19	0.27	10	10
65	00065	6.62	0.01	276.58 ± 74.49	0.06 ± 0.04	0.95 ± 0.17	0.09	8	10
69	00069	7.05	0.19	131.07 ± 32.19	0.19 ± 0.07	0.95 ± 0.18	0.09	14	14
74	00074	8.66	0.15	111.87 ± 46.38	0.04 ± 0.03	0.95 ± 0.23	0.26	3	4
74	00074	8.66	0.15	105.13 ± 29.95	0.05 ± 0.02	0.95 ± 0.16	0.24	9	9
140	00140	8.34	0.15	82.63 ± 20.19	0.09 ± 0.07	0.95 ± 0.18	0.37	7	7
144	00144	7.91	0.17	131.36 ± 33.30	0.05 ± 0.01	0.95 ± 0.17	0.31	10	10
147	00147	8.70	0.15	144.68 ± 47.63	0.03 ± 0.02	0.95 ± 0.19	0.11	6	6
147	00147	8.70	0.15	119.59 ± 37.39	0.04 ± 0.02	0.95 ± 0.18	0.20	9	9
160	00160	9.08	0.15	69.62 ± 13.23	0.07 ± 0.04	0.95 ± 0.14	0.58	20	21
212	00212	8.28	0.15	132.58 ± 48.48	0.05 ± 0.03	0.95 ± 0.20	0.16	5	5
212	00212	8.28	0.15	129.09 ± 40.48	0.05 ± 0.04	0.95 ± 0.19	0.17	7	7
253	00253	10.30	0.15	50.35 ± 17.16	0.04 ± 0.02	0.95 ± 0.24	0.43	16	16
284	00284	10.05	0.11	54.47 ± 20.59	0.04 ± 0.03	0.95 ± 0.23	0.21	11	11
284	00284	10.05	0.11	56.81 ± 15.15	0.04 ± 0.01	0.95 ± 0.16	0.25	23	23

Note. Objects in this table do not have previously published diameters and albedos by the *NEOWISE* team. Beaming η, H, G, the amplitude of the 4.6 μm light curve (W2 amp.), and the numbers of observations used in the 3.4 μm (n_{W1}) and 4.6 μm (n_{W2}) wavelengths are also reported. For a small (<1%) fraction of objects, diameter fits could not reproduce optical magnitudes for a realistic range of albedos. This may be due to a large light curve amplitude, uncertainty in G slope values used to derive H magnitudes, or other reasons noted in Mainzer et al. (2011b, 2012), Masiero et al. (2011, 2012). These objects are marked with a † in the name column. Objects without reported albedos did not have measured H values, see text for details. Only the first 15 lines are shown.

(This table is available in its entirety in machine-readable form.)

Table 5
Measured Diameters (d) and Albedos (p_V) of MBA and Mars Crossers Previously Characterized Using *NEOWISE* Data

Name	Packed	H	G	d (km)	p_V	η	W2 Amp.	n_{W1}	n_{W2}
13	00013	6.74	0.15	202.64 ± 50.08	0.06 ± 0.03	0.95 ± 0.16	0.32	9	9
24	00024	7.08	0.19	151.82 ± 49.32	0.08 ± 0.04	0.95 ± 0.20	0.20	15	15
30	00030	7.57	0.15	93.51 ± 23.53	0.26 ± 0.15	0.95 ± 0.21	0.39	13	13
33	00033	8.55	0.33	48.78 ± 9.98	0.25 ± 0.13	0.95 ± 0.19	0.41	15	15
34	00034	8.51	0.15	114.12 ± 43.76	0.04 ± 0.02	0.95 ± 0.24	0.17	21	22
35	00035	8.50	0.15	143.02 ± 55.51	0.03 ± 0.03	0.95 ± 0.21	0.34	11	11
36	00036	8.46	0.15	102.44 ± 31.81	0.05 ± 0.02	0.95 ± 0.19	0.21	10	10
36	00036	8.46	0.15	92.34 ± 39.98	0.06 ± 0.05	0.95 ± 0.25	0.30	6	6
38	00038	8.32	0.15	114.16 ± 28.20	0.05 ± 0.01	0.95 ± 0.16	0.13	14	14
40	00040	7.00	0.15	95.55 ± 17.94	0.32 ± 0.09	0.95 ± 0.16	0.26	12	12
40	00040	7.00	0.15	107.07 ± 19.23	0.29 ± 0.10	0.95 ± 0.16	0.25	23	23
41	00041	7.12	0.10	198.74 ± 61.71	0.05 ± 0.07	0.95 ± 0.20	0.13	19	19
45	00045	7.46	0.07	181.92 ± 59.39	0.05 ± 0.03	0.95 ± 0.21	0.14	11	11
47†	00047	7.84	0.16	107.18 ± 33.79	0.07 ± 0.03	0.95 ± 0.20	0.28	14	14
48†	00048	6.90	0.15	165.38 ± 41.80	0.06 ± 0.03	0.95 ± 0.15	0.42	11	11

Note. Objects in this table have previously reported measurements by the *NEOWISE* team (Masiero et al. 2011, 2012). Previous measurements use detections in 12 and 22 μm bands, and therefore are better constrained. H, G, beaming η, the amplitude of the 4.6 μm light curve (W2 amp.), and the numbers of observations used in the 3.4 μm (n_{W1}) and 4.6 μm (n_{W2}) wavelengths are also reported. For a small (<1%) fraction of objects, diameter fits could not reproduce optical magnitudes for a realistic range of albedos. This may be due to a large light curve amplitude, uncertainty in G slope values used to derive H magnitudes, or other reasons noted in Mainzer et al. (2011b, 2012), Masiero et al. (2011, 2012). These objects are marked with a † in the name column. Only the first 15 lines are shown.

(This table is available in its entirety in machine-readable form.)

dominated until after the fit was performed. Comparison of those results to *NEOWISE* fits using 12 μm images and radar data confirmed that the thermal fits were poor, so we did not include results that had more than 25% reflected light in the 4.6 μm band.

We assumed that η was equal to the average value for the object's population, as determined by Mainzer et al. (2011b) or Masiero et al. (2011), respectively. For NEAs, this meant $\eta = 1.4 \pm 0.5$; for all other asteroids in this paper, $\eta = 0.95 \pm 0.25$. As shown in Masiero et al. (2011), although the average η

for the main belt is 1.0, the peak of the histogram is located closer to 0.95, so this value was adopted in this work.

Following the average values determined by Mainzer et al. (2011b) and Masiero et al. (2011), the ratio of infrared to visible albedo p_{IR}/p_V was initially set to 1.6 ± 1.0 for NEAs and 1.5 ± 0.5 for Mars-crossers and MBAs. Additionally, it was assumed that the albedos of each band were equal, or $p_{3.4\,\mu m} = p_{4.6\,\mu m}$. Although this may be a poor assumption for objects with red slopes (Grav et al. 2012b), it is necessary to prevent over fitting of the data.
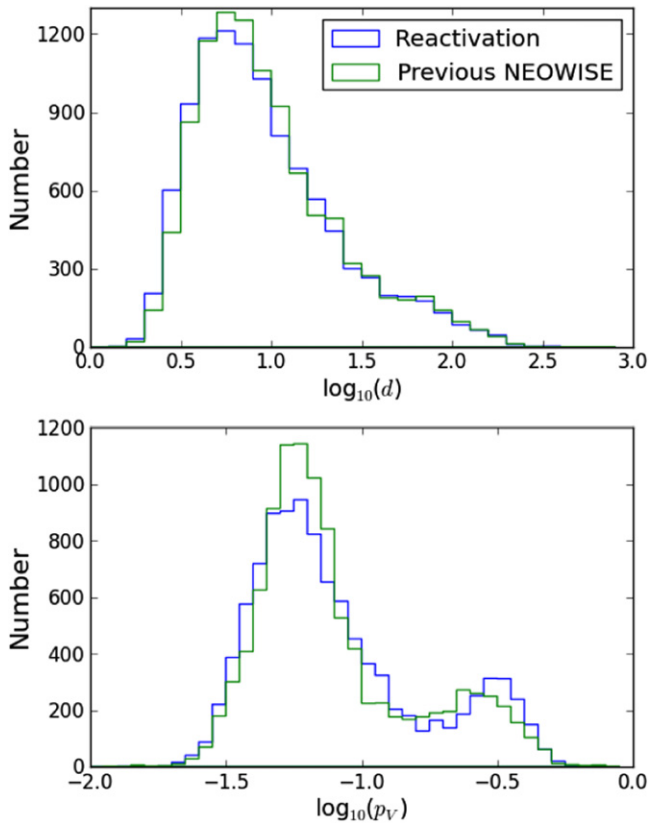
Figure 3. Histogram of MBA diameters (top) and albedos (bottom) measured in this work (blue), and values for the same objects measured by the *NEOWISE* team previously (green). The two albedo peaks are due to the predominance of bright S-type ($p_V = 0.25$) and dark C-type ($p_V = 0.06$) objects in the Main Belt.

Table 6
Measured Diameters and Albedos for Three Objects Using the Model of Wright (2007)

Name	D (km)	p_V
68267	0.89 ± 0.27	0.38 ± 0.32
138127	0.94 ± 0.15	0.35 ± 0.08
285944	1.37 ± 0.23	0.34 ± 0.08

2.3. Uncertainties

Uncertainties on d, p_V, and η (when η was a free parameter) were determined using a Monte Carlo method. Measured *NEOWISE* magnitudes, H, and G were randomly adjusted within their errors, and the resultant model values of d, p_V, and (in appropriate cases) η, were compared to the best-fit values. This process was repeated 25 times for each object, and the resultant errors are the weighted standard deviation of the Monte Carlo trials. The errors quoted in the tables below only include the random component measured through this MC method, not the systematic offset.

Systematic errors were computed by comparing the match between diameters derived in this work to radar-derived diameters for the same objects. Albedos were derived from the radar diameters using the equation

$$d = \frac{1329}{\sqrt{p_V}} 10^{-H/5} \tag{3}$$

where d is the diameter in kilometers (for more information, see Harris & Lagerros 2002).

2.4. Objects without Visible-wavelength Detections

Some MBA and Mars-crossing asteroids had no visible-wavelength measurements available from the MPC. Unlike NEAs, objects determined to have these orbits by the MPC are not added to the MPC's NEO Confirmation Page. Therefore, optical follow-up of these objects is rare, and usually serendipitous. For objects without reported optical detections, the H values in MPCORB.dat represent estimates, not measurements, and p_V could not be derived. Since thermally emitted light weakly depends on albedo, d measurements are reported for these objects. However, lacking targeted follow-up, these objects have short arcs and relatively large position uncertainties, which can add additional systematic errors to the derived diameters.

2.5. NEAs

NEAs were examined with particular care. Objects with poor agreement between observed and modeled H values were refitted with a parameter that tightened the constraints between modeled and observed H. Finally, in some cases an assumption of fixed $\eta = 1.4$ produced a poor result. For NEAs with poor fits, beaming was varied between 1.0 and 2.0, to see if a statistically significant improvement in fit to the observed *NEOWISE* magnitudes could be achieved.

3. RESULTS

Results are divided into four tables. As diameters were calculated using different parameters for the NEAs vs the MBAs and Mars-crossing asteroids, results for these two groups are presented separately. Results are further subdivided between objects that were characterized previously by the *NEOWISE* team, and objects that were not. This is because previously published values likely used the fully cryogenic 12 and 22 μm wavelengths, and therefore can derive diameters more accurately, to within 10%. Researchers looking for the best-constrained diameter and albedo measurements should consult previously published work (Mainzer et al. 2011b, 2012; Masiero et al. 2011, 2012). However, for those researchers who are interested in diameters and albedos derived from additional epochs of data provided by the Year One Reactivation results, we also include the diameters derived for objects using these new data.

Tables 2 and 3 contain the fit diameters and albedos for 173 new and 28 previously characterized NEAs, respectively. Tables 4 and 5 contain the fit diameters and albedos for 1176 new and 6579 previously characterized MBAs and Mars crossing asteroids, respectively. Several objects were observed at multiple apparitions; in these cases, results are presented for each apparition.

Results were compared to previous work by the *NEOWISE* team (Mainzer et al. 2011b, 2012; Masiero et al. 2011, 2012). Figure 3 shows the comparison between diameter and albedo measurements of MBAs. As observed in Masiero et al. (2011), asteroids in the Main Belt group into bright and dark types, with a greater fraction of bright objects found in the inner regions of the belt. Objects that were also modeled with the thermophysical model of Wright (2007) are given in Table 6.
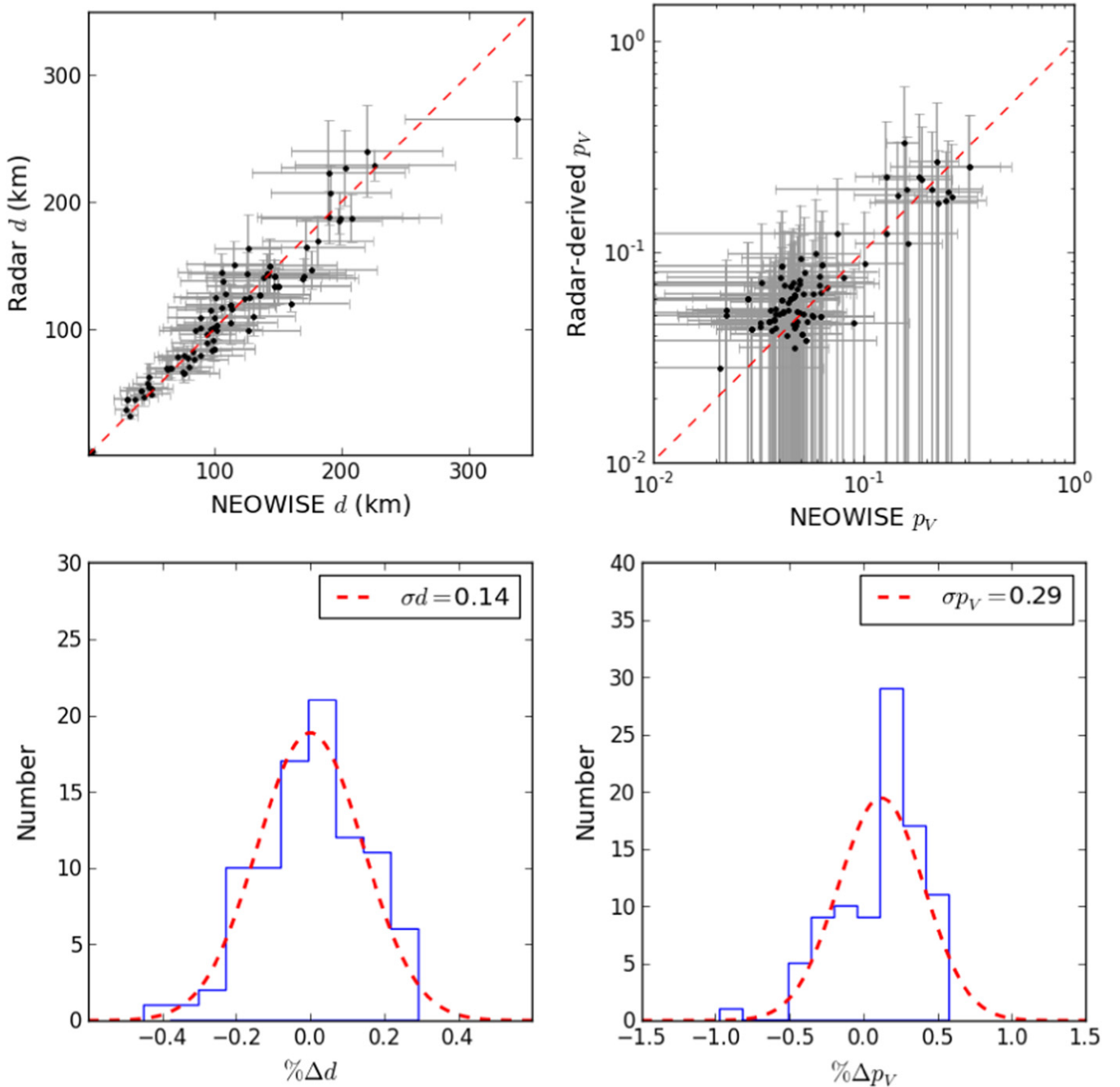
Figure 4. Top: comparison of radar-derived diameters and albedos to the values derived in this paper. The dashed red line shows a 1:1 relation. Bottom: %Δd (left) and %Δp_V (right) are the fractional differences between the *NEOWISE* Reactivation radar-derived diameters and albedos, respectively. The dashed red line is best-fit Gaussian, with the fitted σ given in the legends.

When possible, derived diameters were compared to diameter measurements made from radar data. Radar-derived diameters are ideal for this purpose, as they are derived via an independent method (Benner et al. 2015). This comparison is shown in Figure 4. Although the histograms in the figure are not perfectly Gaussian, a best-fit Gaussian to their forms gives fitted σ values, which indicates a 14% relative accuracy in diameter, and a 29% relative accuracy in albedo. These values are consistent with previous *NEOWISE* 3-band data results (Mainzer et al. 2012; Masiero et al. 2012). From this comparison to radar-derived diameters and previous work, we conclude that diameters are determined to an accuracy of

$\sim$20% or better. If good-quality *H* magnitudes are available, albedos can be determined to within $\sim$40% or better.

Roughly 3% of objects in this work have significantly different derived diameters than previously published *NEO-WISE* values. It is possible that some of these objects are elongated. *NEOWISE* collects a sparsely sampled lightcurve for each object, and for example, it is possible that the prime mission happened to observe one of these objects in a more edge-on shape, whereas the reactivation observations tended to observe a wider side of the object. Alternatively, changes in viewing geometry between epochs could result in different diameter measurements; a pole-on viewing geometry could
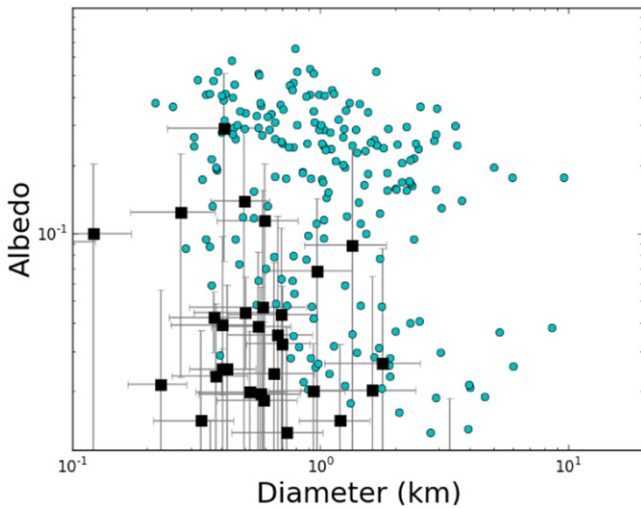
Figure 5. *NEOWISE* detects large NEAs, and discoveries tend to be dark. Cyan circles are measured diameters and albedos of objects detected in the first year of *NEOWISE*'s Reactivation mission; black squares indicate NEAs discovered by *NEOWISE*. Error bars on detected objects are omitted for clarity.

Table 7
Measured Diameters and Albedos for Objects that Meet NHATS Criteria. Also Included are the Minimum Round Trip Time in Days, as Determined by the Barbee et al. (2013) Study

Name	D (km)	p_V	Minimum Round Trip (days)
1943 Anteros	2.30 ± 0.05	0.17 ± 0.02	354
35107	1.00 ± 0.15	0.34 ± 0.10	354
363505	1.90 ± 0.05	0.03 ± 0.01	314
387733	0.33 ± 0.05	0.44 ± 0.15	354
419624	0.35 ± 0.13	0.09 ± 0.15	362

have a larger cross section than a geometry aligned with the plane of the equator.

For a small (<1%) fraction of objects, diameter fits could not reproduce optical magnitudes for a realistic range of albedos. This may be due to a large light curve amplitude (see column $W2$ amp. for the amplitude of the 3.4 μm band light curve, though note that this is a sparsely sampled light curve), uncertainty in G slope values used to derive H magnitudes, or other reasons noted in Mainzer et al. (2011b, 2012), Masiero et al. (2011, 2012). Poor-quality H values can drive albedo fits to extremes; therefore very low (∼0.01) measurements may be signs of this phenomenon.

We have plotted the diameters and albedos of *NEOWISE* Year One Reactivation discoveries, along with all NEAs detected by *NEOWISE* (Figure 5). The trend observed in Mainzer et al. (2014) is also present here: *NEOWISE* tends to discover darker NEAs than optical surveys. This is a direct consequence of the infrared wavelengths that *NEOWISE* employs.

3.1. NHATS Targets

Five objects in this paper meet the NEO Human Space Flight Accessible Targets Study qualifications (Barbee et al. 2013). These objects are listed in Table 7. If an object was observed over multiple epochs, values of d and p_V in this table are the averages of the values and associated errors derived at each of those epochs. Asteroid 419624 was discovered in 2010 by *NEOWISE*.

4. CONCLUSION

We present preliminary diameters and albedos for 7956 asteroids observed in the first year of the *NEOWISE* Reactivation mission. Five of these objects are NHATS targets. Future work by the *NEOWISE* team includes preliminary characterization results from the continuing mission.

Uncertainties on d and p_V are consistent with the errors measured during the initial post-cryo mission. *NEOWISE* is expected to maintain this pace of detection and NEO discovery for the extent of its mission, currently expected to run through 2017. These results demonstrate the power of infrared survey telescopes to characterize basic physical parameters for large numbers of small bodies.

REFERENCES

Barbee, B. W., Abell, P. A., Adamo, D. R., et al. 2013, in IAA Planetary Defense Conf. Proc. (Paris: IAA)
Bauer, J. M., Grav, T., Blauvelt, E., et al. 2013, ApJ, 773, 22
Benner, L., Busch, M. B., Giorgini, J. D., Taylor, P. A., & Margot, J. L. 2015, in Asteroids IV, ed. P. Michel et al. (Tucson, AZ: Univ. of Arizona Press)
Brown, T. M., Baliber, N., Bianco, F. B., et al. 2013, PASP, 125, 1031
Bus, S. J., & Binzel, R. P. 2002, Icar, 158, 146
Carruba, V., Domingos, R. C., Nesvorný, D., et al. 2013, MNRAS, 433, 2075
Cruikshank, D. P. 1977, Icar, 30, 224
Cutri, R. M., Mainzer, A., Conrow, T., et al. 2015, Explanatory Supplement to the NEOWISE Data Release Products, 1, http://wise2.ipac.caltech.edu/docs/release/neowise/expsup
Cutri, R. M., Wright, E. L., Conrow, T., et al. 2012, 1, http://wise2.ipac.caltech.edu/docs/release/allsky/expsup/sec8_1.html
Delbó, M., Harris, A. W., Binzel, R. P., Pravec, P., & Davies, J. K. 2003, Icar, 166, 116
Delbó, M., Walsh, K., Mueller, M., Harris, A. W., & Howell, E. S. 2011, Icar, 212, 138
Gradie, J., & Tedesco, E. 1982, Sci, 216, 1405
Grav, T., Mainzer, A. K., Bauer, J. M., Masiero, J. R., & Nugent, C. R. 2012a, ApJ, 759, 49
Grav, T., Mainzer, A. K., Bauer, J. M., Masiero, J. R., & Nugent, C. R. 2012b, ApJ, 759, 49
Grav, T., Mainzer, A. K., Bauer, J., et al. 2011, ApJ, 742, 40
Grav, T., Mainzer, A. K., Bauer, J., et al. 2012c, ApJ, 744, 197
Hansen, O. L. 1976, AJ, 81, 74
Harris, A. W. 1998, Icar, 131, 291
Harris, A. W., & Lagerros, J. S. V. 2002, in Asteroids III, Botthe, Jr.., et al. (Tucson, AZ: Univ of Arizona Press), 205
Lebofsky, L. A., Veeder, G. J., Lebofsky, M. J., & Matson, D. L. 1978, Icar, 35, 336
Mainzer, A., Bauer, J., Cutri, R. M., et al. 2014, ApJ, 792, 30
Mainzer, A., Bauer, J., Grav, T., et al. 2011a, ApJ, 731, 53
Mainzer, A., Grav, T., Bauer, J., et al. 2011b, ApJ, 743, 156
Mainzer, A., Grav, T., Masiero, J., et al. 2011c, AJ, 736, 100
Mainzer, A., Grav, T., Masiero, J., et al. 2012, ApJL, 760, L12
Mainzer, A., Usui, F., & Trilling, D. E. 2015, in Asteroids IV, ed. P. Michel et al. (Tuscon, AZ: Univ. of Arizona Press)
Masiero, J. R., DeMeo, F., Kasuga, T., & Parker, A. H. 2015, in Asteroids IV, ed. P. Michel et al. (Tuscon, AZ: Univ. of Arizona Press)
Masiero, J. R., Grav, T., Mainzer, A. K., et al. 2014, ApJ, 791, 121
Masiero, J. R., Mainzer, A. K., Bauer, J. M., et al. 2013, ApJ, 770, 7
Masiero, J. R., Mainzer, A. K., Grav, T., et al. 2011, ApJ, 741, 68
Masiero, J. R., Mainzer, A. K., Grav, T., et al. 2012, ApJL, 759, L8
Matter, A., Delbó, M., Ligori, S., Crouzet, N., & Tanga, P. 2011, Icar, 215, 47
McMillan, R. S. 2007, in IAU Symp. 236, ed. G. B. Valsecchi, D. Vokrouhlický, & A. Milani (Cambridge: Cambridge Univ. Press), 329
Milani, A., Cellino, A., Knežević, Z., et al. 2014, Icar, 239, 46
Morrison, D., & Lebofsky, L. 1979, in Radiometry of Asteroids, ed. T. Gehrels (Tucson, AZ: Univ. of Arizona Press)
Müller, T. G., Miyata, T., Kiss, C., et al. 2013, A&A, 558, A97
Müller, T. G., O'Rourke, L., Barucci, A. M., et al. 2012, A&A, 548, A36
Ostro, S. J., Hudson, R. S., Benner, L. A. M., et al. 2002, in Asteroids III, ed. W. F. Botthe Jr. et al. (Tuscon, AZ: Univ. of Arizona Press), 205
Pravec, P., Harris, A. W., Kušnirák, P., Galád, A., & Hornoch, K. 2012, Icar, 221, 365
Tedesco, E. F., Noah, P. V., Noah, M., & Price, S. D. 2002, AJ, 123, 1056
Tholen, D. J., Mainzer, A. K., Bauer, J. M., et al. 2014, MPEC, 145
Walsh, K. J., Delbó, M., Bottke, W. F., Vokrouhlický, D., & Lauretta, D. S. 2013, Icar, 225, 283
Williams, G. V. 2012, PhD thesis, Open Univ. UK
Wolters, S. D., Green, S. F., McBride, N., & Davies, J. K. 2005, Icar, 175, 92
Wolters, S. D., Green, S. F., McBride, N., & Davies, J. K. 2008, Icar, 193, 535
Wright, E. L. 2007, arXiv:astro-ph/0703085
Wright, E. L., Eisenhardt, P. R. M., Mainzer, A. K., et al. 2010, AJ, 140, 1868
Zellner, B. 1979, in Asteroids, ed. T. Gehrels (Tucson, AZ: Univ. of Arizona Press), 78